A triangular finite element with local remeshing for the large strain analysis of axisymmetric solids

Walter B. Castelló, Fernando G. Flores *

Department of Structures, National University of Córdoba and CONICET, Casilla de Correo 916, 5000 Córdoba, Argentina

ABSTRACT

In this work, a three-node triangular finite element with two degrees of freedom per node for the large strain elasto-plastic analysis of axisymmetric solids is presented. The formulation resorts to the adjacent elements to obtain a quadratic interpolation of the geometry over a patch of four elements from which an average deformation gradient is defined. Thus, the element formulation falls within the framework of assumed strain elements or more precisely of **F**-bar type formulations. The in-plane behavior of the element is similar to the linear strain triangle, but without the drawbacks of the quadratic triangle, e.g. contact or distortion sensitivity. The element does not suffer of volumetric locking in problems with isochoric plastic flow and the implementation is simple. It has been implemented in a finite element code with explicit time integration of the momentum equations and tools that allow the simulation of industrial processes. The widely accepted multiplicative decomposition of the deformation gradient in elastic and plastic components is adopted here. An isotropic material with non-linear isotropic hardening has been considered. Two versions of the element have been implemented based on a Total and an Updated Lagrangian Formulation, respectively. Some approximations have been considered in the latter formulation aimed to reduce the number of operations in order to increase numerical efficiency. To consider bulk forming, with large geometric changes, an automatic local remeshing strategy has been developed. Several examples are considered to assess the element performance with and without remeshing.

© 2008 Elsevier B.V. All rights reserved.

1. Introduction

The finite element analysis of the bulk forming processes, including rolling, forging, extrusion, etc. is relatively complex because it implies important changes in the original geometry, large strains, isochoric plastic flow, interaction (contact) with the forming tools and in many cases, self-contact and a strong thermo-mechanical coupling. When large strains are involved the use of low order elements with only displacements degrees of freedom is preferred as they are more reliable and robust. For problems than can be simulated as bidimensional this leads to linear triangles and bilinear quadrilaterals. It is well known that when these elements are based on a standard displacement formulation they are vulnerable to volumetric locking. Besides that, specially in the case of triangles, very fine meshes are necessary to obtain accurate results. Considerable efforts have been made in recent years to bypass these drawbacks. For the bilinear quadrilateral the developments have been quite successful leading to elements that do not lock for quasi-incompressible problems and show a good approxi-

mation for coarse meshes. The formulations used, including reduced/selected integration, the addition of incompatible modes, **B**-bar methods and assumed/enhanced strain methods, may be seen in [1–4] and the references cited therein.

However, although meshing programs using quadrilaterals have notably improved, the triangles are more convenient for general applications as the triangular mesh generators are more robust and efficient, facilitating the development of automatic remeshing strategies for highly distorted geometries. This has motivated the development of triangular elements introducing drilling degrees of freedom [5], mixed/hybrid formulations [6–9] and **F**-bar type formulations [10]. The first approach is restricted to small strain plane stress problems (as part of a shell element), the second is presently restrained to small strains also and the others, although eliminate the volumetric locking problem, do not improve the poor behavior of the linear triangle. A promising approach, that keeps displacements as the only degrees of freedom and improves the in-plane behavior was presented in [11], where the strains are computed resorting to the geometry of the adjacent elements. This approach will be extended in this paper. The use of a patch of elements for the computation of strains is not new and has been previously considered mainly for C^1 problems. Probably the first successful applications were under energy formulations in the

* Corresponding author. Tel./fax: +54 351 433 4144.
E-mail addresses: wcastello@efn.uncor.edu (W.B. Castelló), fflores@efn.uncor.edu (F.G. Flores).

finite difference context by Bushnell [12] (see also [13]) and in the finite element context by Barnes [14]. In the last 15 years several shell elements have been developed using this idea (see for example [15] and the references cited therein).

For large strain elasto-plastic problems, the constitutive models based on the multiplicative decomposition of the deformation gradient are now widely accepted. This broad consensus emerges from the microstructural theory of monocrystal and, at least for isotropic materials, there is no controversy referred to the definition of the intermediate configuration that characterizes the hypothesis. Examples of constitutive models and computational algorithms to integrate the resulting evolution equations based on this hypothesis may be found in Refs. [16–21] among others.

In bulk forming processes, most of the problems of interest imply large changes in geometry, making necessary to apply a remeshing strategy and a data transfer scheme. It is of paramount importance that these strategies keep the finite element solution within a prescribed accuracy. Different algorithms for transfer of variables have been proposed, among them those based on the *Superconvergent Patch Recovery* (SPR) method introduced in [22,23] are frequently used. In this algorithm a global approximation of the variables in the domain is obtained with a polynomial expansion over a set or patch of elements. This polynomial expansion approaches (via least squares) the values provided by the finite element analysis at some points of the patch that have superconvergent properties. The original algorithm has been modified by different authors [24–26] improving different aspects, e.g. include balance equation in the patch, increase the robustness of the interpolation at boundary points, etc. leading to the so-called *Enhanced Superconvergent Patch Recovery* methods. Although the procedure is heuristic, it has been tested enough to admit that the results are quite accurate; see for example Ref. [27] and more recently Ref. [28]. The first authors to apply the SPR algorithm to elasto-plastic problems were Boroomand and Zienkiewicz [29] and among the applications in the finite strain range Refs. [30,31] may be cited.

In this paper, a three-node triangular element for the analysis of bidimensional (plane strain and axisymmetric) isotropic solids with an elasto-plastic constitutive model based on the multiplicative decomposition of the deformation gradient is developed. Both a Total Lagrangian Formulation (TLF) and an Updated Lagrangian Formulation (ULF) have been considered. In the former a standard model as presented in Ref. [18] is used while in the latter the approach suggested in Ref. [17] to increase the computational efficiency reducing the number of operations at the element level was implemented. The element was coded in the finite element program Stampack [32]. An automatic strategy to trigger local remeshing including a transfer scheme based on the original *Superconvergent Patch Recovery* [22,23] was implemented.

An outline of this work is as follows. Next section describes the constitutive models used and the numerical algorithms adopted to integrate the evolution equations for both the TLF and the ULF. The finite element and the assumed strain approach developed is presented in Section 3. The local remeshing scheme is summarized in Section 4, that also includes some comments about the transfer of internal variables. Several examples solved with the new element are presented in Section 5 including cases with and without remeshing and comparisons with other results existing in the literature. Finally some conclusions are gathered at the end of the paper.

2. Constitutive model

In this section, the main aspects of the elasto-plastic constitutive model and of the two integration algorithms used in this work for the analysis of solids under large strains are summarized. The first algorithm, associated to a TLF, is very similar to one in the monograph [18], the details of it and several numerical examples may be found in [33]. The second algorithm, associated to an ULF, is based on Ref. [17]. For the element presented in this paper both formulations show comparative advantages and disadvantages. The ULF requires to recompute the average derivatives of the shape functions at each iteration but avoids some expensive push-forward/pull-back type operations.

2.1. Hypothesis associated to the material model

The domain occupied by the solid in its original/undeformed configuration in the space $\mathbb{R}^3$ will be denoted by Ω_0 with boundary Γ_0 (see Fig. 1). A function $\varphi(\mathbf{X}, t)$ relating, at every time t, the material points $\mathbf{X}$ on the reference configuration Ω_0 with the present/deformed configuration Ω_t will be defined, such that it is possible to obtain the deformation gradient as:

$$\mathbf{F}(\mathbf{X}, t) = \frac{\partial \varphi(\mathbf{X}, t)}{\partial \mathbf{X}}. \tag{1}$$

Fig. 1 shows schematically the different configurations involved in the multiplicative decomposition of the deformation gradient. Besides the original Ω_0 and the present configuration Ω_t, the figure also includes the additional stress-free *intermediate configuration* (denoted by $^i\Omega_t$).

The basic kinematic hypothesis is the multiplicative decomposition of the deformation gradient $\mathbf{F}$ in an elastic part $\mathbf{F}^e$ and a plastic one $\mathbf{F}^p$ according to

$$\mathbf{F} = \mathbf{F}^e\mathbf{F}^p, \tag{2}$$

where it is also assumed that the plastic part does not modify the volume (isochoric plastic flow), then $\det(\mathbf{F}^p) = 1$ and $\det(\mathbf{F}) = \det(\mathbf{F}^e) = J$. This multiplicative decomposition is uniquely defined but for a rigid body rotation and expression (2) is enough to define without ambiguities the unstressed intermediate configuration for isotropic materials, that is the type of material model considered here. From the elasticity point of view the elastic deformations will be computed via an hyperelastic relationship and it will be assumed that the strain energy can be decoupled into a part due to the change of volume and a part due to the distortion of the solid. For simplicity it will also be assumed that is feasible to fix a linear relationship between adequate strain and stress measures in terms of a bulk modulus K and a shear modulus μ. The yield function will be assumed to depend on the second invariant of the deviatoric stress tensor J_2 only. An associative flow rule with isotropic hardening will be considered so that a radial return algorithm can be applied to get back to the yield surface when plasticity occurs. Finally rate independent plasticity, no thermo-mechanical coupling and an isothermal process will be assumed.

2.2. Integration algorithm

As in most of the elasto-plastic algorithms (see for example Ref. [19] or [18]), the problem is decomposed in two parts: an elastic
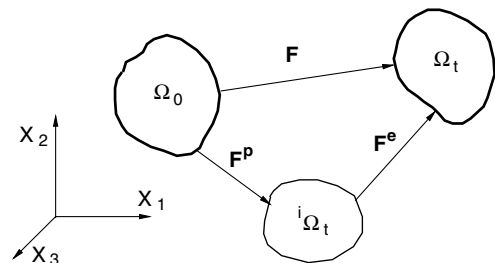

Fig. 1. Configurations considered in the multiplicative decomposition.

part where the plastic variables are frozen (elastic predictor) and a plastic part where the total strains are kept fixed (plastic corrector), in such a way that the combination of both problems is equivalent to the original one.

A few details pertaining to the kinematic of the configurations shown in Fig. 2 are given. The present configuration is associated to the step $n + 1$ and is obtained adding the configuration in step n and the incremental displacements $\mathbf{u}_n$:

$$\mathbf{x}_{n+1} = \varphi_{n+1}(\mathbf{X}) = \varphi_n(\mathbf{X}) + \mathbf{u}_n[\varphi_n(\mathbf{X})], \tag{3}$$

where for the integration of the constitutive equations, the configuration $\varphi_n(\mathbf{X})$ at step n and the incremental displacements $\mathbf{u}_n$ are data. According to Fig. 2 and using (3), the *total deformation gradient* at the present step $\mathbf{F}_{n+1}$ can be obtained as

$$\mathbf{F}_{n+1} = \frac{\partial \mathbf{x}_{n+1}}{\partial \mathbf{X}} = [\mathbf{1} + \nabla_{x_n} \mathbf{u}_n] \mathbf{F}_n \tag{4}$$

with $\mathbf{1}$ the second order unit tensor. Using the chain rule

$$\mathbf{F}_{n+1} = \frac{\partial \mathbf{x}_{n+1}}{\partial \mathbf{X}} = \frac{\partial \mathbf{x}_{n+1}}{\partial \mathbf{x}_n} \frac{\partial \mathbf{x}_n}{\partial \mathbf{X}} = \mathbf{f}_{n+1} \mathbf{F}_n \tag{5}$$

allows to define the *relative gradient* $\mathbf{f}_{n+1}$ as

$$\mathbf{f}_{n+1} = \frac{\partial \mathbf{x}_{n+1}}{\partial \mathbf{x}_n} = \mathbf{F}_{n+1} \mathbf{F}_n^{-1} = \mathbf{1} + \nabla_{x_n} \mathbf{u}_n. \tag{6}$$

Depending on the formulation used, it may be found more convenient to use the inverse of the relative deformation gradient $\mathbf{f}_{n+1}^{-1}$ that can be computed simply as

$$\mathbf{f}_{n+1}^{-1} = \frac{\partial \mathbf{x}_n}{\partial \mathbf{x}_{n+1}} = \mathbf{1} - \nabla_{x_n} \mathbf{u}_n, \tag{7}$$

where expression (7) can be easily obtained from (4).

Total Lagrangian Formulation: From the decomposition (2) the trial elastic part of the deformation gradient can be computed as

$$\mathbf{F}_{n+1}^{e\,trial} = \mathbf{F}_{n+1} \mathbf{F}_n^{p\,-1} \tag{8}$$

representing the point of departure of the algorithm. Performing the spectral decomposition of the elastic right Cauchy–Green tensor $\mathbf{C}^e$ we have:

$$\mathbf{C}_{n+1}^{e\,trial} = \left(\mathbf{F}_{n+1}^{e\,trial}\right)^T \left(\mathbf{F}_{n+1}^{e\,trial}\right) = \left(\mathbf{U}_{n+1}^{e\,trial}\right)^2 = \sum_{i=1}^{3} \left(\lambda_i^{trial}\right)_{n+1}^2 \mathbf{r}_i \otimes \mathbf{r}_i, \tag{9}$$

where λ_i^{trial} and $\mathbf{r}_i$ are the eigenvalues and eigenvectors, respectively, of the elastic right stretch tensor $\mathbf{U}_{n+1}^{e\,trial}$. This allows to introduce an elastic logarithmic strain measure over the intermediate configuration with components of the form

$$e_i^{e\,trial} = \ln\left(\lambda_i^{trial}\right) \tag{10}$$

$\mathbf{F}_n$
Ω_0
Ω_n
$\mathbf{F}_n^{\mathbf{p}}$
$\mathbf{F}_n^{\mathbf{e}}$
$^i\Omega_n$
X_2
$\mathbf{F}_{n+1}$
$\mathbf{F}_{n+1}^{\mathbf{e}\,trial}$
f_{n+1}
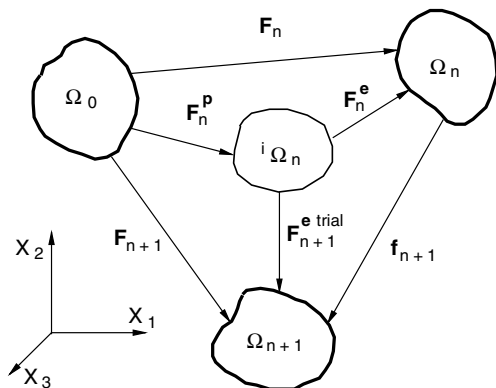X_1
Ω_{n+1}
X_3

Fig. 2. Configurations considered in the integration of the constitutive model.

and a conjugated stress measure $\mathbf{O}$, that can be split in volumetric and deviatoric components:

$$\mathbf{O}_{n+1}^{trial} = K\ln(J)\mathbf{1} + 2\mu\,\mathrm{dev}(\mathbf{e}_{n+1}^{e\,trial}) = p\mathbf{1} + \mathbf{o}^{trial}. \tag{11}$$

Using the standard *radial return algorithm* for $J_2(\mathbf{o})$ plasticity, the updated internal variables $(\mathbf{F}_{n+1}^{p\,-1}, e_{n+1}^p)$ can be computed. The stress tensor $\mathbf{O}$ and the second Piola–Kirchhoff stress tensor referred to the intermediate configuration $\overline{\mathbf{S}}$, are related through the elastic part of the right stretch tensor $\mathbf{U}^e$:

$$\overline{\mathbf{S}} = (\mathbf{U}^e)^{-1} \mathbf{O} (\mathbf{U}^e)^{-1}. \tag{12}$$

It can be seen in Fig. 2 that to obtain a stress measure over the original configuration a plastic pull back transformation is necessary:

$$\mathbf{S} = (\mathbf{F}^p)^{-1} \overline{\mathbf{S}} (\mathbf{F}^p)^{-T}. \tag{13}$$

This stress measure can be used to write the weak form of the momentum equations as

$$\delta\Pi = \int_{\Omega_0} [\delta\mathbf{E}_{GL} : \mathbf{S}]d\Omega_0 + \delta\Pi_{ext} = 0, \tag{14}$$

where $\mathbf{E}_{GL}$ is the Green–Lagrange strain tensor:

$$\mathbf{E}_{GL} = \frac{1}{2}(\mathbf{F}^T\mathbf{F} - \mathbf{1}). \tag{15}$$

Updated Lagrangian Formulation: Again, the point of departure is the multiplicative decomposition of the deformation gradient (2) and the chain rule in (5) that allows to write the trial elastic component as

$$\mathbf{F}_{n+1}^{e\,trial} = \mathbf{f}_{n+1}\mathbf{F}_n^e. \tag{16}$$

For the ULF it is more convenient to use a spatial strain measure. The last equation allows to define the elastic Finger tensor, to be used as internal variable, as

$$\left(\mathbf{b}_{n+1}^e{}^{-1}\right)^{trial} = \mathbf{f}_{n+1}^{-T}(\mathbf{b}_n^e)^{-1}\mathbf{f}_{n+1}^{-1} \tag{17}$$

and the corresponding elastic Almansi strain tensor:

$$\mathbf{e}_{n+1}^{e\,trial} = \frac{1}{2}\left[\mathbf{1} - \left(\mathbf{b}_{n+1}^e{}^{-1}\right)^{trial}\right]. \tag{18}$$

Assuming, in this case a linear relation between the Kirchhoff stress tensor and the elastic Almansi strain tensor (which for metals is fully justified), we can write

$$\tau_{n+1}^{trial} = K\,\mathrm{tr}\left[\mathbf{e}_{n+1}^{e\,trial}\right]\mathbf{1} + 2\mu\,\mathrm{dev}\left[\mathbf{e}_{n+1}^{e\,trial}\right], \tag{19}$$

where the elastic deviatoric strains are $\mathrm{dev}\left[\mathbf{e}_{n+1}^e\right] = -\frac{1}{2}\mathrm{dev}\left[\mathbf{b}_{n+1}^e{}^{-1}\right]$, that together with (19) allow to write the trial deviatoric part of the Kirchhoff stress tensor as

$$\mathbf{s}_{n+1}^{trial} = -\mu\,\mathrm{dev}\left[\left(\mathbf{b}_{n+1}^e{}^{-1}\right)^{trial}\right]. \tag{20}$$

The simplicity of J_2 plasticity allows to consider a classical radial return algorithm to obtain the corrected stresses and internal variables $\left(\mathbf{b}_{n+1}^e{}^{-1}, e_{n+1}^p\right)$. Using the Kirchhoff stress tensor, the weak form of the momentum equations on the present configuration can now be written as

$$\delta\Pi = \int_{\Omega_{n+1}} \delta\varepsilon : \tau\,d\Omega_{n+1} + \delta\Pi_{ext} = 0, \tag{21}$$

where ε is the usual infinitesimal strain tensor. The main advantage of the ULF summarized above is the reduction in the number of operations necessary to integrate the constitutive equation at each Gauss point. Note that the spectral decomposition of $\mathbf{C}$ implicit in

(9) or the transformations (12) and (13) are avoided. For a typical problem the ULF requires 30% less of CPU time than the TLF.

Note that for TLF and the ULF the linear relation between elastic strains and stresses is applied over different stress/strain measures. Because of that, slight differences in the results obtained with both formulations are expected. The results obtained with the TLF will be assumed as the reference values in the numerical experiments below.

3. Finite element approximation

Low order elements are preferred when large distortion occurs (large strain range) and also when interaction between bodies (contact) is involved. Due to the strong and combined non-linearities standard implicit codes may show unsolvable convergence problems. Because of that most of the commercial finite element programs intended to metal forming simulations use pseudo static solutions obtained through the explicit integration of critically damped dynamic equations. For fully explicit algorithms degrees of freedom other than displacements, like pressure that have no associated mass, require special integration algorithms which lead to a certain loss in efficiency: e.g. it may be necessary a double loop over each integration point or a smaller time increment [9]. These aspects are the motivation for the approximation developed next, an extension of a triangular element presented in [11], that includes only translational displacement as degrees of freedom.

3.1. Geometry mapping

The point of departure of this approach is a domain discretized with three-node triangles, but now, in contrast with the standard displacement approach for linear triangles, the computation of the strains at each element is made considering the geometry of the three surrounding elements too.

Fig. 3a shows the patch of four elements defined by the central element "*C*", where the strains are to be computed, and the three adjacent elements. The same patch of elements is shown in Fig. 3b but now in the usual parametric space where, for the central element, the same nodal positions of the standard linear element are kept, and the positions occupied by the extra nodes and elements can be seen.

The patch of four triangular elements is defined by six nodes, and although it has been formed adding linear triangles, it allows to define a quadratic interpolation of the geometry. The corresponding shape functions N^I can be obtained imposing conditions $N^I(\xi^J, \eta^J) = \delta_{IJ}$ in a standard way, where δ_{IJ} is the Kronecker delta. These functions have been listed in Table 1 where the coordinate $\zeta = 1 - \xi - \eta$ has been included.

The goal of this quadratic interpolation is to define an assumed strain approach that allows to avoid volumetric locking on one

Fig. 3. Patch of triangular elements. (a) Spatial coordinates and (b) natural coordinates.

Table 1
Quadratic shape functions over the patch of elements

$N^1 = \zeta + \xi\eta$	$N^2 = \xi + \eta\zeta$	$N^3 = \eta + \zeta\xi$
$N^4 = \frac{\zeta}{2}(\zeta - 1)$	$N^5 = \frac{\xi}{2}(\xi - 1)$	$N^6 = \frac{\eta}{2}(\eta - 1)$

hand and to improve the in-plane behavior on the other. Denoting by $\mathbf{X}^I$ and $\mathbf{x}^I$ the nodal coordinates in the reference (undeformed) configuration and in an arbitrary (deformed) configuration, respectively, and with $\mathbf{u}^I$ the corresponding displacements, we have

$$\mathbf{X} = \sum_{I=1}^{6} N^I \mathbf{X}^I, \tag{22a}$$

$$\mathbf{x} = \sum_{I=1}^{6} N^I \mathbf{x}^I = \sum_{I=1}^{6} N^I (\mathbf{X}^I + \mathbf{u}^I). \tag{22b}$$

It must be noted that the element results *non-conforming*, i.e. the interpolations of the geometry along the common boundary of two elements leads to different values, because the quadratic interpolations are independent for each patch as they are written in terms of different nodes (different patches). As shown in Ref. [11] this non-conformity has no important consequence and the element passes the patch test.

A very important aspect of this quadratic interpolation is that when the deformation gradient is computed at the center of each side of the central element (points denoted as G_i in Fig. 3b) the contributions of the nodes that do not belong to the two adjacent elements vanish. Consider for example the mid-point of side 2-3 (G_1) between the central element "*C*" and element "1", the nodes that do not belong to any of these elements are nodes 5 and 6. If we compute the derivatives of the associated shape functions (see Table 1), we have

$$N^5_{,\xi} = \xi - \frac{1}{2}, \quad N^5_{,\eta} = 0, \tag{23a}$$

$$N^6_{,\xi} = 0, \quad N^6_{,\eta} = \eta - \frac{1}{2} \tag{23b}$$

it can be easily seen that these derivatives vanish at the side center ($\xi = \eta = \frac{1}{2}$), i.e. the gradient depends only on the position of nodes 1–4. This property makes these points excellent candidates to be used in an assumed strain approach, because the same deformation gradient will be computed at these points independently from both adjacent elements.

3.2. Computation of strains

In the original element [11] the right Cauchy–Green deformation tensor $\mathbf{C}$ computed at mid-side points is linearly interpolated in the element. In this work, as a multiplicative decomposition of the deformation gradient $\mathbf{F}$ will be used for the constitutive model, the deformation gradient computed at each side center will be interpolated instead. Let us see some details:

The Jacobian matrix of the quadratic mapping (22a) at each mid-side points G_i is

$$\mathbf{J}^0_i = \frac{\partial \mathbf{X}}{\partial \boldsymbol{\xi}}(\xi_i) = \sum_{I=1}^{6} N^I_{,\xi}(\xi_i) \mathbf{X}^I, \tag{24}$$

$$\mathbf{J}_i = \frac{\partial \mathbf{x}}{\partial \boldsymbol{\xi}}(\xi_i) = \sum_{I=1}^{6} N^I_{,\xi}(\xi_i) \mathbf{x}^I, \tag{25}$$

where $\boldsymbol{\xi} = (\xi, \eta)$, the lower index i means computed at G_i and the upper index 0 means computed at the original configuration. The expressions (24) and (25) allow to evaluate the in-plane components of the deformation gradient at those points:
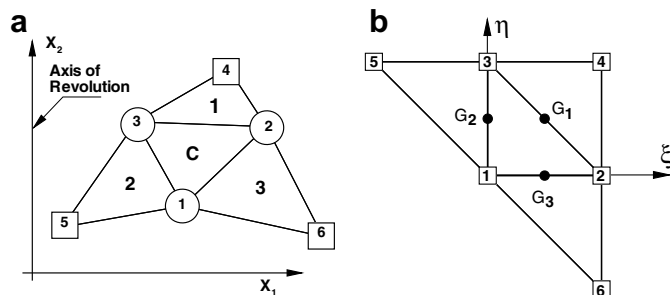
$$\mathbf{F}_i = \frac{\partial \mathbf{x}}{\partial \mathbf{X}}(\xi_i) = \frac{\partial \mathbf{x}}{\partial \xi} \frac{\partial \xi}{\partial \mathbf{X}}(\xi_i) = \mathbf{J}_i(\mathbf{J}_i^0)^{-1} \tag{26a}$$

$$= \sum_{I=1}^{6} N_{,\xi}^I(\xi_i) \, (\mathbf{J}_i^0)^{-1} \mathbf{x}^I \tag{26b}$$

$$= \sum_{I=1}^{6} N_{,\mathbf{X}}^I(\xi_i) \mathbf{x}^I. \tag{26c}$$

With the aim to have an efficient finite element, one integration point per element will be used. For that an average deformation gradient is defined as

$$\overline{\mathbf{F}} = \frac{1}{V} \int_V \mathbf{F} \, dV, \tag{27}$$

where the integrals are computed numerically using the G_i points as sampling points. For plane strain problems this leads simply to the average of the deformation gradients computed on each mid-side point:

$$\overline{\mathbf{F}} = \frac{1}{3} \sum_{i=1}^{3} \mathbf{F}_i, \tag{28}$$

while for axisymmetric problems (with $X_1 = $ radius and $X_{1i} = X_1(\xi_i)$) the average deformation gradient results:

$$\overline{\mathbf{F}} = \frac{2\pi \int_A \mathbf{F} X_1 \, dA}{2\pi \int_A X_1 \, dA} = \frac{\sum_{i=1}^{3} X_{1i} \mathbf{F}_i}{\sum_{j=1}^{3} X_{1j}} \tag{29}$$

than can also be seen as a weighted average, using the radius of each point X_{1i} as weighting factor. The average gradient $\overline{\mathbf{F}}$ results:

$$\overline{\mathbf{F}} = \frac{\sum_{i=1}^{3} X_{1i} \sum_{I=1}^{6} N_{,\mathbf{X}}^I(\xi_i) \mathbf{x}^I}{\sum_{j=1}^{3} X_{1j}} \tag{30a}$$

$$= \sum_{I=1}^{6} \frac{\sum_{i=1}^{3} N_{,\mathbf{X}}^I(\xi_i) X_{1i}}{\sum_{j=1}^{3} X_{1j}} \mathbf{x}^I \tag{30b}$$

$$= \sum_{I=1}^{6} \overline{N}_{,\mathbf{X}}^I \mathbf{x}^I. \tag{30c}$$

If a TLF is used, the last expression shows that it is possible to obtain weighted Cartesian derivatives of the nodal shape functions ($\overline{N}_{,\mathbf{X}}^I$) with respect to the reference configuration. This simplifies the computation of the average deformation gradient $\overline{\mathbf{F}}$ because the derivatives ($\overline{N}_{,\mathbf{X}}^I$) are invariant during the process and can be computed only once.

The weighted deformation gradient in (30a) includes only the in-plane components. For plane strain the stretch of a fiber normal to the plane (direction X_3) is simply $\lambda_3 = 1$. For axisymmetric problems different approaches may be considered as long as the element obtained is free from volumetric locking. One possibility is to use linear approximations on each element of the patch for the evaluation of the normal stretch at their centers, and to compute a weighted average of these stretches. Good results have been obtained using the average between the stretch at the central element and the average of the stretches in the adjacent elements. Denoting by

$(\lambda_3)_C$ the stretch at the central element C computed in standard form from the coordinates of its three nodes

$$(\lambda_3)_C = \frac{\sum_{I=1}^{3} L^I x_1^I}{\sum_{I=1}^{3} L^I X_1^I} \tag{31}$$

$(\lambda_3)_{1-3}$ the average of the stretches computed in the adjacent elements

$$(\lambda_3)_{1-3} = \frac{1}{3} \sum_{i=1}^{3} \frac{\sum_{I=1}^{3} L^I x_1^{I(i)}}{\sum_{J=1}^{3} L^J X_1^{J(i)}}, \tag{32}$$

where L^I are the standard linear triangular functions (area coordinates) and $x_1^{I(i)}$ indicates the radius at local node I of adjacent element i. Giving values at the center of each element $L^I(\xi = \eta = \frac{1}{3})$ the average out-of-plane stretch results:

$$\overline{\lambda}_3 = \frac{(\lambda_3)_C + (\lambda_3)_{1-3}}{2} \tag{33a}$$

$$= \frac{1}{2} \left\{ \frac{\sum_{I=1}^{3} x_1^I}{\sum_{I=1}^{3} X_1^I} + \frac{1}{3} \left(\sum_{J=1}^{3} \frac{\sum_{K=1}^{3} x_1^{K(J)}}{\sum_{K=1}^{3} X_1^{K(J)}} \right) \right\} \tag{33b}$$

$$= \sum_{I=1}^{6} M^I x_1^I, \tag{33c}$$

where the M^I are constants that can be also computed at the beginning of the process.

When the adjacent element to side i is missing (domain boundary), the above expressions can not be applied directly and may be modified as follows:

- For the computation of the in-plane components of the deformation gradient on the mid-side point $\mathbf{F}_i$, use the usual expressions of the constant strain triangle (CST). In the implementation, this can also be done defining a fictitious position for the inexistent node $(I + 3)$ (see Fig. 4)

$$\mathbf{x}^{I+3} = \frac{\mathbf{x}^J + \mathbf{x}^K}{2} + \left(\frac{\mathbf{x}^J + \mathbf{x}^K}{2} - \mathbf{x}^I \right) = \mathbf{x}^J + \mathbf{x}^K - \mathbf{x}^I \tag{34}$$

transferring the contributions according to

$$\delta \mathbf{u}^{I+3} = \delta \mathbf{u}^J + \delta \mathbf{u}^K - \delta \mathbf{u}^I. \tag{35}$$

Note that these four points $(I, J, I + 3, K)$ define a parallelogram with a constant Jacobian matrix that is equal to the Jacobian matrix computed from the three nodes of element C. Note also that for a side along the axis of symmetry the radius is null and is then null its contribution to the average gradient.

- For the out-of-plane component, use again the above average between λ_C and λ_{1-3}, but for the latter averaging include only the existing adjacent elements (if only two adjacent element exist, $\overline{\lambda}_3$ results from the average between $(\lambda_3)_C$ and the average stretch of the two adjacent elements).

In the numerical experiments it has been detected that when an element has only one adjacent element (two of its sides are part of the boundary), the gradient averaging alleviates the volumetric locking but does not eliminate it completely. Because of that, whenever possible, the nodal connectivities of such elements are modified automatically within the computational code so that they have two adjacent elements. Note that in the code, once the three-node triangular mesh have been input, before any computation the four-triangle patches must be formed, i.e. the adjacent elements
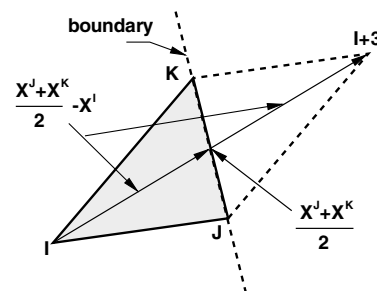

Fig. 4. Definition of a ficticious node at the solid boundary.

have to be detected. It is at this stage when element connectivities may be modified.

If an ULF is used, the above expressions (30a) and (33a) require $\overline{N}^l_{,\mathbf{x}}$ and M^l to be computed each time the reference configuration is updated. If the update is performed at every step and the algorithm for the constitutive model described above is used, it is more convenient to compute the inverse of the relative gradient between the configuration at the previous step (n) and the present configuration ($n+1$)

$$\mathbf{f}^{-1} = \frac{\partial \mathbf{x}_n}{\partial \mathbf{x}_{n+1}} = \sum_{I=1}^{6} \overline{N}^l_{\mathbf{x}_{n+1}} x^l_n, \tag{36}$$

where x^l_n are the nodal coordinates at the previous step and the derivatives $\overline{N}^l_{\mathbf{x}_{n+1}}$ are obtained with expressions identical to (30a). In a similar fashion, using (33a), the relative normal stretch between both configurations can be obtained.

3.3. $\boldsymbol{B}$-bar matrix

Once the stresses have been evaluated for any of the two Lagrangian formulations, the equivalent nodal forces are computed from the virtual work expression (14) or (21).

3.3.1. Total Lagrangian Formulation
The variation of the Green–Lagrange strains is

$$\delta \mathbf{E}_{GL} = \frac{1}{2}(\mathbf{F}^T \delta \mathbf{F} + \delta \mathbf{F}^T \mathbf{F}) \tag{37}$$

that can be displayed as

$$\delta \begin{bmatrix} E_{11} \\ E_{22} \\ 2E_{12} \\ E_{33} \end{bmatrix} = \sum_{I=1}^{6} \begin{bmatrix} \overline{N}^l_{,1} \overline{\mathbf{F}}^T_1 \\ \overline{N}^l_{,2} \overline{\mathbf{F}}^T_2 \\ \overline{N}^l_{,2} \overline{\mathbf{F}}^T_1 + \overline{N}^l_{,1} \overline{\mathbf{F}}^T_2 \\ \bar{\lambda}_3 [M^l, 0] \end{bmatrix} [\delta \mathbf{u}^l] = \overline{\mathbf{B}}_{TL} \delta \mathbf{u}^p, \tag{38}$$

where $\overline{\mathbf{F}}_i$ is the column i of $\overline{\mathbf{F}}$ and $\delta \mathbf{u}^p$ includes the virtual displacements of the six nodes in the patch.

Note again that the average derivatives $\overline{N}^l_{,i}$ and the factors M^l have been computed at the start of the process.

3.3.2. Updated Lagrangian Formulation
The variation of the small strain tensor ε is

$$\delta \varepsilon = \frac{1}{2}(\nabla_{\mathbf{x}_{n+1}} \delta \mathbf{u} + \nabla^T_{\mathbf{x}_{n+1}} \delta \mathbf{u}) \tag{39}$$

that can be written as

$$\delta \begin{bmatrix} \varepsilon_{11} \\ \varepsilon_{22} \\ 2\varepsilon_{12} \\ \varepsilon_{33} \end{bmatrix} = \sum_{I=1}^{6} \begin{bmatrix} \overline{N}^l_{,1} & 0 \\ 0 & \overline{N}^l_{,2} \\ \overline{N}^l_{,2} & \overline{N}^l_{,1} \\ \bar{\lambda}_3 M^l & 0 \end{bmatrix} [\delta \mathbf{u}^l] = \overline{\mathbf{B}}_{UL} \delta \mathbf{u}^p, \tag{40}$$

where the average derivatives $\overline{N}^l_{,i}$ and the factors M^l have to be recomputed at each iteration using (30a) and (33a) with current configuration coordinates.

4. Adaptive remeshing strategy

An automatic remeshing strategy allows to analyze problems including large distortions and important changes in the geometry. It comprises two main aspects that must be considered in detail: the generation of the new mesh and the transfer of variables between the old and the new mesh. The latter aspect is particularly relevant for the history-dependent variables as is the case of the internal variables of the constitutive model.

4.1. Automatic zone remeshing

Remeshing techniques are intended to avoid large aspect ratios in order to maintain an adequate approximation level. They generally imply the replacement of all the elements in the domain of interest at each remeshing stage. Such a strategy has some drawbacks, among them: (a) the transfer of variables imply some loss of information (e.g.: some gradients may be locally smoothed) (b) normally the new (unstructured) mesh has a larger number of elements than the original mesh. In order to improve these aspects, a possible solution is to remesh only a zone of the domain, i.e. the part where the element distortion is above a certain threshold. It is then proposed to replace only the most distorted elements (and the surroundings ones) with new elements of similar size but with a more regular shape. The most relevant aspects are to establish an adequate measure of the element distortion and to develop an algorithm for the selection of the elements to be included in the zone to be remeshed.

There are different measures of the distortion in triangular elements. Perhaps the most widely used is to compare the inner angles of the deformed triangle with the inner angles in the undeformed triangle (see Fig. 5b and c). These ratios will be used in this work.

The remeshing stage is automatically triggered when the distortion ratio β at any element satisfies:

$$\beta = \min\left(\frac{\alpha^n_j}{\alpha^0_j}\right) < d_{\min}, \tag{41}$$

where α^0_j is the original angle at node j and α^n_j is the angle at node j at current configuration (step n) (see Fig. 5). In Eq. (41) the maximum allowable distortion ratio is defined by the parameter $d_{\min}$. The elements to be replaced are those than satisfy $\beta < d_{\max}$ where $d_{\max}$ is higher than $d_{\min}$, in this way all the elements that show a certain degree of distortion will be replaced and not only those that have arrived to the critical value. Very good results have been obtained using the pair of parameters $[d_{\min}, d_{\max}] = [1/3, 2/3]$.

For bidimensional solids the boundary of the zone to be remeshed is a closed line. The most important aspects in the definition of this boundary are

- To distinguish correctly which part of the zone boundary belongs to the body boundary and which part is an inner boundary. This is important because the nodes in the inner boundary
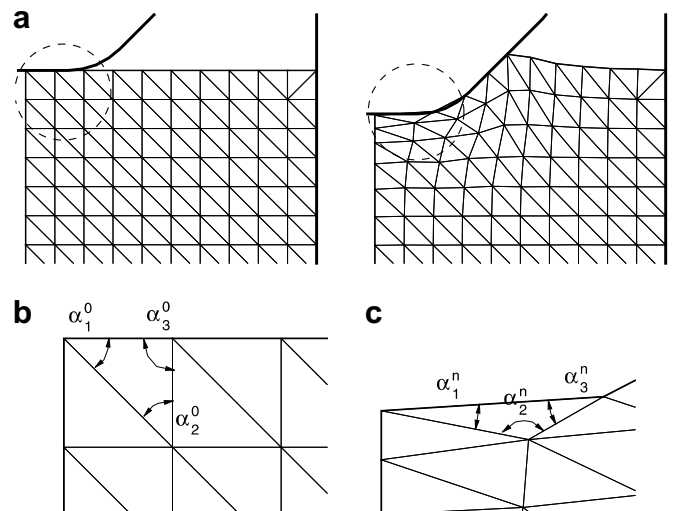

Fig. 5. Mesh distorsion for finite strain processes. (a) Initial inner angles and (b) distorsion of the triangular element and inner angles at time n.

must be kept as they also belong to the elements in the non-remeshed part (see Fig. 6a). Fortunately this is an straightforward task because the present element formulation requires the information of the neighbor elements.

- To avoid the existence of loops (see Fig. 6b). To accomplish this, taking advantage again of the information of each element neighbors, it is found convenient that if an element satisfies the condition to be remeshed then all its adjacent elements are also included in the zone to be remeshed.

- Finally, the element distortions normally lead to the existence of external boundary segments with lengths quite different from the uniform side length prescribed for the mesh generation. When these segments are too long (specially in contact conditions), they should be divided accordingly as the results may show low precision. When these segments are too short they should be merged, if not the new mesh will show small elements (see Fig. 6c) that have a deleterious influence in the critical time used for explicit time integrators, leading to larger CPU times.

The generation of the new mesh with the prescribed element size, including the boundary conditions is performed with the software GiD [34] using the *batch file* options.

4.2. Transfer of variables

The algorithm used for variable transfer between meshes is based on the original SPR [22,23] and the proposal by Akin [36]. This technique shows an important capability to interpolate variables accurately from superconvergent points which are normally coincident with element integration points.

4.2.1. Updated Lagrangian Formulation

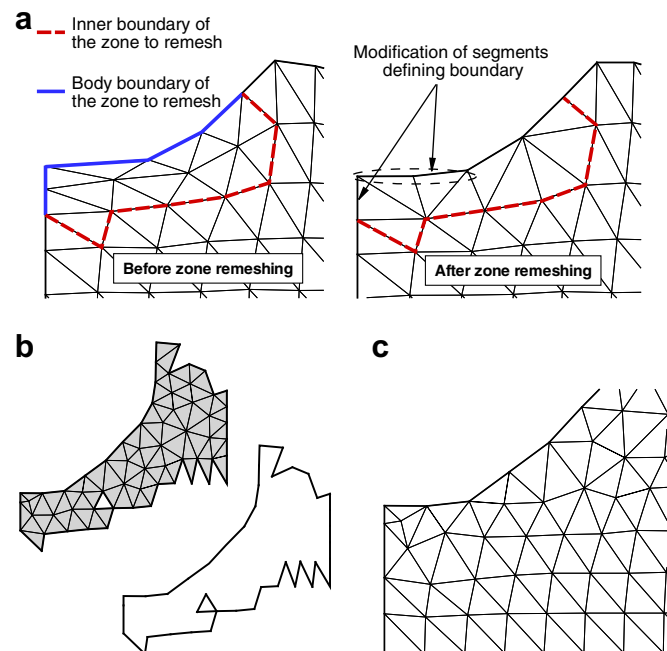If the reference configuration is updated at every step, the internal variables of the constitutive model are defined over the de-formed configuration. As a consequence, the internal variables $\{e^p, \mathbf{b}^{e-1}\}$ can be directly transferred. Alternatively it is possible to transfer the Kirchhoff stress tensor and to recompute tensor $\mathbf{b}^{e-1}$ from it. This later approach has the advantage that deviatoric stresses may be scaled after the transfer to satisfy the von-Mises equivalent stress existent before the transfer.

4.2.2. Total Lagrangian Formulation

The internal variables of the constitutive model are the (scalar) equivalent plastic strain e^p and the inverse of the plastic deformation gradient $\mathbf{F}^{p-1}$. The Cartesian components of the latter can not b interpolated from different Gauss points because $\mathbf{F}^{p-1}$ is not unequivocally defined (is not invariant to a rotation $\mathbf{R}$ of the intermediate configuration). It is then more convenient to transfer spatial variables that are invariant under a rotation of the intermediate configuration and we have chosen to transfer the Kirchhoff stress tensor τ. Once the transfer of τ is performed it is possible to recover the internal variables ($\mathbf{F}^{p-1}$) to continue with the elastic plastic process. Besides that the new mesh becomes the reference configuration (it is not a TLF any longer) and the deformation gradient is now computed relative to the remeshed configuration. Then at every new stage we have $\mathbf{F} = \mathbf{1} = \mathbf{F}^e \mathbf{F}^p = \mathbf{U}^e \mathbf{F}^p$, then:

$$\mathbf{F}^{p-1} = \mathbf{U}^e(\tau). \tag{42}$$

Note that in this case the plastic deformation gradient includes a volumetric component associated to the elastic volumetric strain at the present configuration but this has no consequences in the simulation.

5. Numerical results

In this section, a set of numerical results obtained with the formulation described above is presented. Solids undergoing large elasto-plastic strain have been analyzed with special emphasis in axisymmetric problems.

The element described in Section 3 was implemented in the finite element code Stampack [32] that uses an explicit integration of the momentum equations and a penalty formulation for contact. The pseudo static results obtained with the present formulation are identified by the acronym *TR2D*. In all the examples but the second, present results have been compared with those obtained with the software Abaqus/Explicit [37] using the enhanced strain four node quadrilateral with one integration point and hourglass control (*CAX4R*).

The first two examples do not use the remeshing strategy an have been included mainly to compare the results obtained with both (TLF and ULF) the formulations considered and also to compare the present element with other formulations existing in the literature and experimental values. In the third example, the remeshing strategy is used although it is not strictly necessary and allows to compare results with and without remeshing. In the last two examples remeshing is mandatory to arrive to the end of the simulation due to the strong distortion of the mesh. In all the examples the parameters (distortion limits) considered to control remeshing were $[d_{min}, d_{max}] = [1/3, 2/3]$.

All the original configurations of the examples below have four sides and are amenable to be modelled with regular structured meshes. This also helps to easily visualize at each stage of the process the part of the mesh that has not been remeshed yet. The data input for the program includes a flag to automatically (or not) modify connectivities of elements with only one adjacent element. This modification is performed not only on the original mesh (provided by the user) but also on the meshes provided by GiD at each remeshing stage.

Fig. 6. Important aspects in the remesh zone definition. (a) Type of boundary identification; (b) appearance of a possible inner loops and (c) small boundary segments leading to elements of reduced size.

5.1. Elasto-plastic hollow sphere under internal pressure

In this initial, example the elasto-plastic behavior of a thick hollow sphere under internal pressure is considered. The inner radius of the sphere is 0.254 m with a thickness of 0.254 m. Taking account of global symmetry the upper half of the sphere is only modelled. The material is assumed to be aluminium with mechanical properties: Young's modulus $E = 38$ GPa, Poisson's ratio $v = 0.33$, mass density $\rho = 2672$ kg/m^3, initial yield stress $\sigma_y = 27$ MPa and hardening modulus $\sigma'_y = 270$ MPa. The maximum internal pressure is 35 MPa that leads to a full plastification of the sphere. The discretization used is shown in Fig. 7a and includes 64 $(8 \times 4 \times 2)$ triangles. Fig. 7b plots the radial displacement of the points in the inner (upper curves) and outer (lower curves) surfaces. For comparison purposes the plot also includes the results obtained with three elements in software Abaqus [37]; namely, (a) the above mentioned *CAX4R*, (b) *CAX4* a fully integrated four node quadrilateral and (c) *CAX3H* a linear triangle with constant pressure. In the first case results are obtained with Abaqus/Explicit and in the other two with the Abaqus/Standard (implicit) version.

It can be seen that the results provided by the fully integrated quadrilateral *CAX4*, although no exactly equal at all points, are more uniform than those of element *TR2D*, specially along the inner surface. Besides that the results obtained with element *TR2D* are quite better that those obtained with the hybrid triangular element *CAX3H* that shows the improvement of present formulation over other linear triangles. Also note the rather poor performance of element *CAX4R* in this simulation.

5.2. External inversion of a thin-walled tube using a die

This example considers a process that allows to make double walled tubes through the axial compression of a single-walled tube against an adequate die (see Fig. 8). This problem, usually simulated as an impact at low speed (see [38,17,39,4] among others), shows moderately large strains that depend on the opening radius (r_m) of the die. The case considered here was taken from the work of Rosa et al. [39] where experimental results are also reported.

The material of the tube is aluminium with elastic mechanical properties: Young's modulus $E = 69$ GPa, Poisson's ratio $v = 0.3$ and density $\rho = 2700$ kg/m^3. The plastic behavior is governed by the J_2 model with non-linear isotropic hardening given by $\sigma_y = 0.2983 \times (28 \times 10^{-4} + e^p)^{0.086}$ GPa. The friction coefficient between the tube and the die is $\mu = 0.1$.

The mesh includes 480 $(4 \times 60 \times 2)$ triangular elements. The four rows of elements across the thickness are necessary to capture
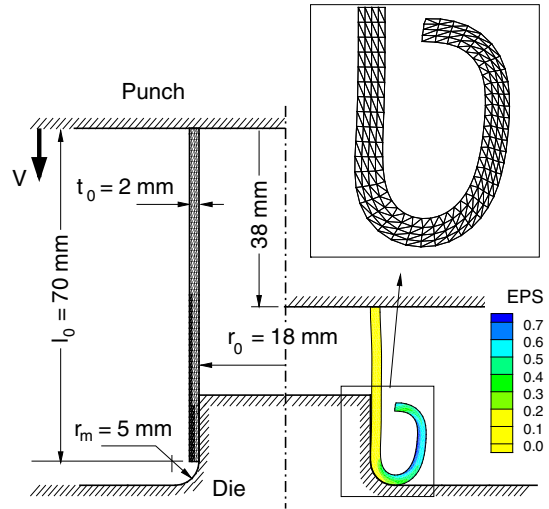

Fig. 8. Inversion of a thin-walled tube. Geometry, discretization and final configuration.
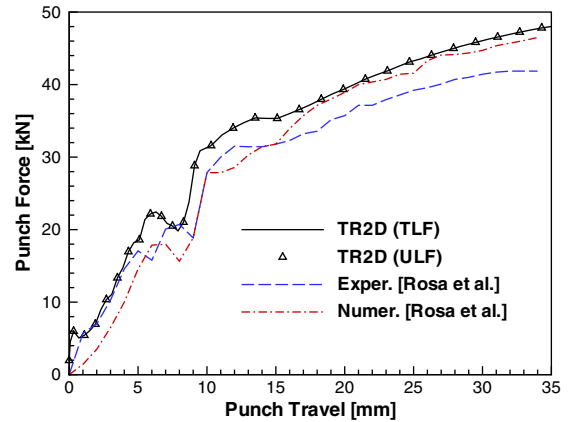

Fig. 9. Inversion of a thin-walled tube. Plot of punch force versus punch displacement.

the details of the forming process. Fig. 8 shows the final deformed geometry and the equivalent plastic strains for the maximum punch travel of 38 mm. Although the distortions are rather low the equivalent plastic strain have a maximum value of 0.8. Fig. 9
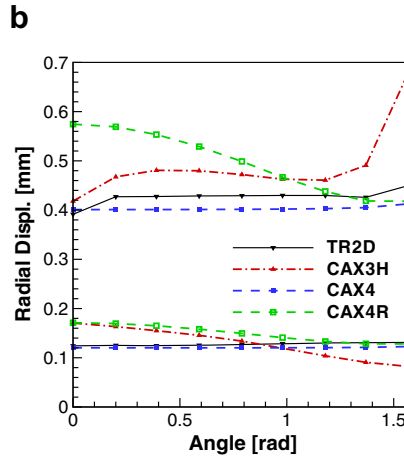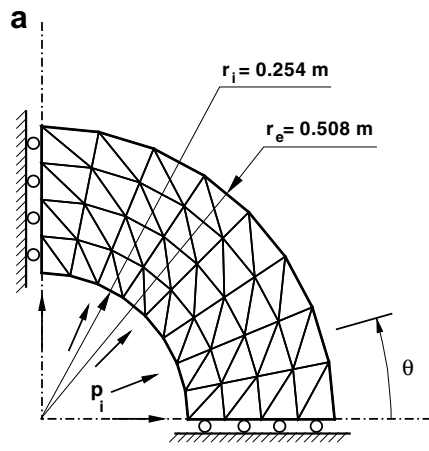

Fig. 7. Expansion of a hollow sphere. (a) Original geometry and discretization and (b) radial displacement of inner and outer surfaces.
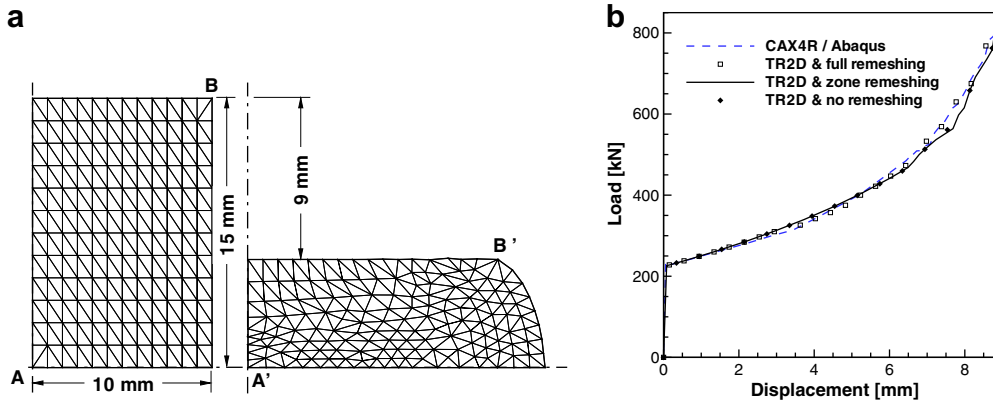
Fig. 10. Upsetting of cylindrical billet. (a) Original geometry and deformed configuration and (b) plot of punch force versus punch travel.

plots the driving force versus the displacement of the top platen. This curve shows a peak of almost 20 kN corresponding to the instant in which the end of the tube has traveled round the curved part of the die. After that the load increases monotonically until the end of the simulation. Compared with the experimental results presented in [39], present results (*TR2D*) show a good agreement at the beginning of the simulations and some differences after the load peak. Compared with the numerical simulations in [39] there are differences at the first part of the process but they are quite close for the second half of the punch travel. There is also a very

Table 2
Upsetting of cylindrical billet

Strategy	e^p_{max}	Time (s)
CAX4R [37]	1.8791	–
TR2D full remeshing	1.8431	13.64
TR2D zone remeshing	1.8471	10.33

Comparison of CPU times and e^p between full and zone remeshing using TR2D.

good agreement with the experimental final deformed geometry (not shown). The results obtained with both formulations (TLF and ULF) presented above are almost coincident as can be seen in the figure.

5.3. Upsetting of a cylindrical billet

This benchmark, defined in Ref. [40], is the forming of a cylindrical billet between two rigid plates that is reduced in length by 60%. The problem involves not only large strains but an important distortion of the mesh, making necessary the application of a remeshing scheme. The specimen is 30 mm long with a radius of 10 mm and is compressed between two flat dies. The material properties are Young's modulus $E = 200$ GPa, Poisson's ratio $v = 0.3$ and the density $\rho = 7833$ kg/m³. A linear isotropic hardening is assumed, with a initial yield stress $\sigma_y = 700$ MPa and a hardening modulus $\sigma'_y = 0.3$ GPa. A non-slip condition of the billet with the tools is assumed (perfectly rough) that is controlled with a high friction coefficient $\mu = 1.0$.
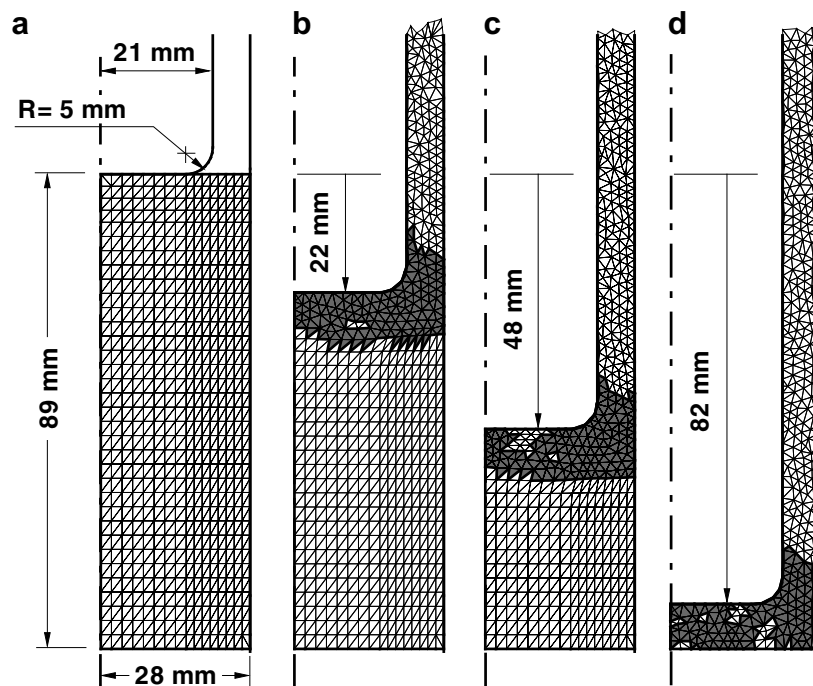

Fig. 11. Back extrusion of a cylindrical billet. (a) Initial geometry and (b–d) deformed configurations for increasing punch travels and details of the remeshed zones.

Only the upper half of the geometry was discretized due to symmetry with an initially structured mesh including 288 ($12 \times 12 \times 2$) triangular elements. The strong change in geometry introduces large mesh distortions mainly along the diagonal $\overline{A'B'}$ than can be seen in Fig. 10a as the remeshed zone.

Only one remeshing stage has been used leading to a mesh with 320 elements. This number is quite below the 400 elements obtained when the whole domain is remeshed [33].

The numerical results obtained with the present formulation have been compared with those obtained with the software Abaqus [37] using the same initial mesh with 144 (12×12) CAX4R elements and an adaptive meshing scheme instead of remeshing.

The curves of reaction force versus vertical displacement of the plate are plotted in Fig. 10b for the elements CAX4R and TR2D, showing practically no differences. Table 2 compares the maximum values of equivalent plastic strain and the CPU time (since remeshing until the end of the simulation) obtained with element TR2D using zone remeshing and full remeshing. The saving in CPU time in this example is of the order of 25% when zone remeshing is used instead of full remeshing.

5.4. Back extrusion of a cylindrical billet

The generation of a tube by back extrusion of a cylindrical billet leads to plastic flow with a very strong geometry change. The original axisymmetric geometry is shown in Fig. 11a. The tools are assumed rigid and the material of the billet is aluminium with Young's modulus $E = 38$ GPa, Poisson's ratio $v = 0.33$ and density $\rho = 2672$ kg/m^3. The plastic behavior is defined by an initial yield stress $\sigma_y = 27$ MPa and linear isotropic hardening with modulus $\sigma_y' = 1.1$ MPa. The contact with the tools is assumed frictionless. The original mesh includes 1088 ($16 \times 34 \times 2$) triangular element. The rigid die is fixed and the punch travels down 82 mm to generate the tube as shown in Fig. 11. For this simulation 22 remeshing stages were used with an average of 1060 elements. Fig. 11b–d shows three different instants of the process when zone remeshing have been performed. The shadowed elements indicate the new elements provided by the mesher [34].

Table 3 shows the maximum equivalent plastic strain and the final length of the tube for the simulations using the present approach (TR2D) and using [37] (CAX4R). The differences may be due to the discretization strategy used by Abaqus that considers a structured mesh with moving nodes (Adaptive Meshing) every 10 steps. This strategy gives very good results for most part of the simulation but in the final steps shows a spurious thinning at the lower part of the tube (see Fig. 12a). Note that the simulation is frictionless, then no vertical forces can developed along the tube. This spurious thinning implies an increase in both the maximum effective plastic strain and in the length of the tube.

Fig. 13. Back extrusion of a cylindrical billet. Punch force versus punch travel.

Fig. 14. Forging of a disk with a sinusoidal die. Original and deformed configurations for different punch travels.

Table 3
Back extrusion of a cylindrical billet

Element	e_{max}^p	L_{max} (mm)
CAX4R [37]	4.080	200.20
TR2D (present)	3.841	196.92

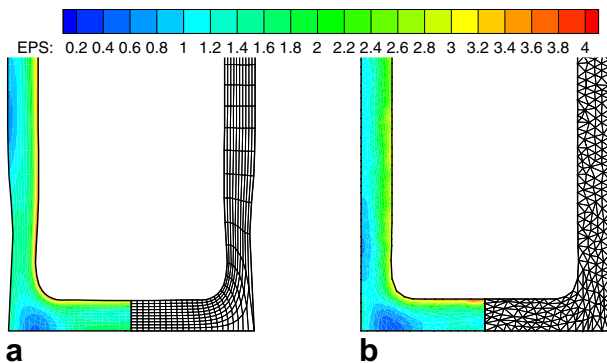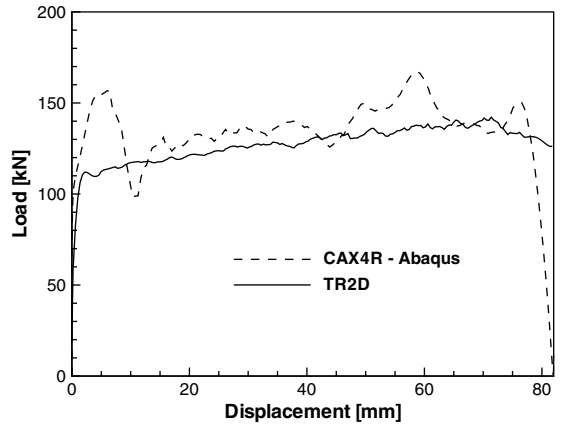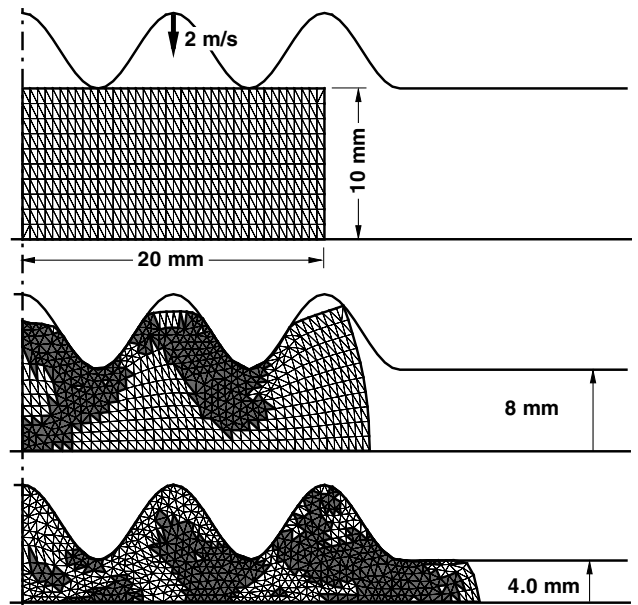Maximum equivalent plastic strain and final tube length.

Fig. 12. Back extrusion of a cylindrical billet. Final deformation and contour fill of the equivalent plastic strain. (a) CAX4R [37] and (b) TR2D (present).

Table 4
Forging of a disk with a sinusoidal die. Maximum equivalent plastic strain and final disk radius

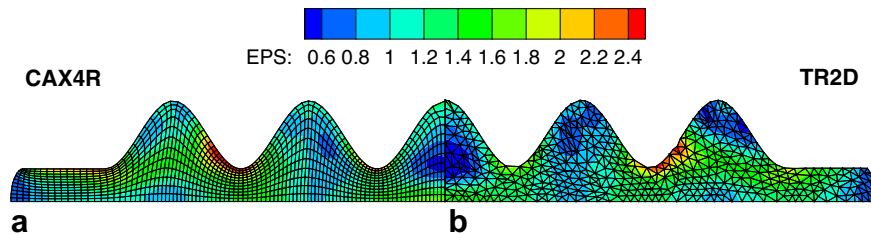| Element	e_{max}^p	r_{max} (mm)
CAX4R [37]	2.625	31.90
TR2D (present)	2.588	31.99

Fig. 15. Forging of a disk with a sinusoidal die. Final deformation and contour fill of the equivalent plastic strain. (a) CAX4R [37] and (b) TR2D (present).

Finally, Fig. 13 plots extrusion force versus punch displacement. The results obtained with element *TR2D* are quite more uniform and do not show the initial peak nor the final decay obtained with element *CAX4R*. These may be due to the awkward original mesh used for element Abaqus necessary to accommodate to the important shape changes keeping a sort of structured mesh.

5.5. Forging with a sinusoidal die

This last example allows to assess the element behavior in forging problems involving complex geometries and an important material flow during the deformation process. The sinusoidal geometry of the upper die considerable restricts the plastic flow causing high mesh distortions and making mandatory a remeshing strategy to carry out the analysis.

The problem (see left part of Fig. 14) consists of a rigid die and a deformable disk 10 mm thick with of radius of 20 mm. The die has a sinusoidal cross sectional shape with an amplitude of 5 mm and a period of 10 mm. The disk is made of steel with Young's modulus $E = 200$ GPa, Poisson's ratio $v = 0.3$, density of $\rho = 7800$ kg/m^3 and linear isotropic hardening defined by an initial yield stress of $\sigma_y = 100$ MPa and a hardening modulus of $\sigma'_y = 300$ MPa. The die moves vertically with a constant velocity of 2 m/s until a total displacement of 7.6 mm.

The lower face of the disk is constrained in the vertical direction and the friction with the lubricated tools is disregarded. The disk has been discretized with 800 ($10 \times 40 \times 2$) triangular elements (451 nodes). Six remeshing stages were used in the analysis with an average of 850 elements. Table 4 shows two representative results using the present element and those obtained with program Abaqus [37] using element *CAX4R* with adaptive remeshing every 5 steps of 6795 total steps. The results obtained are very similar but it may be noted that the mesh used in Abaqus is much finer including 1152 quadrilateral elements and 1261 nodes. The right part of Fig. 15 shows the final deformed mesh of the disk and the contours of equivalent plastic strains.

6. Conclusions

A triangular finite element for the simulation of bidimensional (axisymmetric) solids has been presented. The element is adequate for industrial applications including large strains and important geometrical distortions. The element geometry is defined by three nodes with translational degrees of freedom only and for the computation of the strains (deformation gradient) it is also resorted to the geometry of the adjacent elements. The formulation developed falls into assumed strain type approaches or **F**-bar type. The deformation gradient at each element is computed through a weighted average of the deformation gradients computed at each mid-side of the element using a quadratic interpolation of the geometry over the element and the neighbor ones. The computational implementation of the element is simple and, due the low interpolation order including only displacement degrees of freedom, has advantages in

problems involving contact, adaptive remeshing and explicit integration of the momentum equations.

The element shows a very good behavior in the finite strain range compared with enhanced strain four node quadrilaterals and volumetric locking was not detected in elasto-plastic problems that always includes certain degree of compressibility. The element performance is similar to the linear strain triangle but without the distortion sensitivity and contact problems of the latter.

For the examples included (metals with J_2 plasticity where the hypothesis of small elastic strain is reasonable), as expected, the numerical results do not show remarkable differences between an Updated Lagrangian Formulation and a Total Lagrangian Formulation.

The CPU times of the former are approximately 30% less than the latter due to the important reduction in the number of operations necessary for the integration of the constitutive model. This reduction is specially important in the simulation of industrial processes that are generally very CPU time demanding.

The strategy developed for the mesh improvement involved only the zones of the solid where distortions have grown beyond a certain limit. A simple criterion based on inner angles ratios has been used to define the zone to be remeshed. This local remeshing decreases the loss of information due to transfer of variables, improves mesh regularity and diminish CPU times. In the simulations there are zones that in part of the process do not deform at all or that move as a rigid body. A full remeshing is not only unnecessary but also non-convenient and inaccurate.

All the examples included are axisymmetric because most of the metal forming simulations that can be modelled as 2D problems are of this type. Nevertheless the element and the strategies developed can be applied to plane strain situations. The idea of meshing only the most distorted elements and the criteria used can be immediately extended to 3D problems. In any case a versatile meshing tool that accepts multiple-connected domains and different restrains on the boundary is necessary.

References

[1] J.C. Simo, M.S. Rifai, A class of mixed assumed strain methods and the method of incompatible modes, Int. J. Numer. Methods Engrg. 29 (1990) 1595–1638.
[2] J.M.A. César de Sá, R.M. Natal Jorge, New enhanced strain element for incompressible problems, Int. J. Numer. Methods Engrg. 44 (1999) 229–248.
[3] F. Armero, On the locking and stability of finite elements in finite deformation plane strain problems, Comput. Struct. 75 (2000) 261–290.
[4] L. Adam, J.P. Ponthot, Thermomechanical modeling of metals at finite strains: first and mixed order finite elements, Int. J. Solids Struct. 42 (2005) 5615–5655.
[5] C.A. Felippa, A study of optimal membrane triangles with drilling freedoms, Comput. Methods Appl. Mech. Engrg. 192 (2003) 2125–2168.

[6] R. Mahnken, I. Caylak, G. Laschet, Two mixed finite element formulations with area bubble functions for tetrahedral elements, Comput. Methods Appl. Mech. Engrg. 197 (2008) 1147–1165.

[7] O.C. Zienkiewicz, J. Rojek, R.L. Taylor, M. Pastor, Triangles and tetrahedra in explicit dynamic codes for solids, Int. J. Numer. Methods Engrg. 43 (1998) 565–583.

[8] M. Cervera, M. Chiumenti, Q. Valverde, Agelet de Saracibar C Mixed linear/linear simplicial elements for incompressible elasticity and plasticity, Comput. Methods Appl. Mech. Engrg. 192 (2003) 5249–5263.

[9] J. Rojek, E. Oñate, R.L. Taylor, CBS-based stabilization in explicit solid dynamic, Int. J. Numer. Methods Engrg. 66 (2006) 1547–1568.

[10] E.A. Souza Neto, F.M.A. Pires, D.R.J. Owen, A new F-bar based method for linear triangles and tetrahedra in the finite strain analysis of nearly incompressible solids, in: E. Oñate, D.R.J. Owen (Eds.), Computational Plasticity COMPLAS 2003, CIMNE, Barcelona, Spain, 2003.

[11] F.G. Flores, A two-dimensional linear assumed strain triangular element for finite deformation analysis, ASME J. Appl. Mech. 73 (6) (2006) 970–976.

[12] D. Bushnell, B.O. Almroth, F. Brogan, Finite difference energy methods for nonlinear shell analysis, Comput. Struct. 1 (1971) 361–387.

[13] R.A. Nay, S. Utku, An alternative to the finite element method, Variational Methods Engrg. 1 (3) (1972) 62–74.

[14] Barnes MR. Form Finding and Analysis of Tension Space Structure by Dynamic Relaxation, Ph.D. Thesis, Department of Civil Engineering, The City University, London, 1977.

[15] F.G. Flores, C. Estrada, A rotation-free thin shell quadrilateral, Comput. Methods Appl. Mech. Engrg. 196 (2007) 2631–2646.

[16] A.L. Eterovic, K.J. Bathe, A hyperelastic-based large strain elasto-plastic constitutive formulation with combined isotropic-kinematic hardening using logarithmic stress and strain measures, Int. J. Numer. Methods Engrg. 30 (1990) 1099–1115.

[17] García Garino CG. A Numerical Model for Large Strain Analysis of Elasto-plastic Solids (in Spanish), Ph.D. Thesis, Tech. Univ. of Catalonia, Spain, 1993.

[18] M.A. Crisfield, Non-linear Finite Element Analysis of Solids and Structures II: Advanced Topics, John Wiley & Sons Ltd., 1997.

[19] J.C. Simo, T.J.R. Hughes, Computational Inelasticity, Springer-Verlag Inc., New York, 1998.

[20] A.S. Khan, P. Cheng, An anisotropic elastic–plastic constitutive model for single and polycrystalline metals I, Int. J. Plasticity 12 (1996) 147–162.

[21] A.S. Khan, P. Cheng, An anisotropic elastic–plastic constitutive model for single and polycrystalline metals II, Int. J. Plasticity 14 (1998) 209–226.

[22] O.C. Zienkiewicz, J.Z. Zhu, The superconvergent patch recovery and a posteriori error estimates. Part I: the recovery technique, Int. J. Numer. Methods Engrg. 33 (1992) 1331–1364.

[23] O.C. Zienkiewicz, J.Z. Zhu, The superconvergent patch recovery and a posteriori error estimates. Part II: error estimates and adaptativity, Int. J. Numer. Methods Engrg. 33 (1992) 1365–1382.

[24] N.E. Wiberg, F. Abdulwahab, S. Ziukas, Enhanced supercovergent patch recovery incorporating equilibrium and boundary conditions, Int. J. Numer. Methods Engrg. 37 (1994) 3417–3440.

[25] P. Labbé, A. Garon, A robust implementation of Zienkiewicz and Zhu's local patch recovery method, Commun. Appl. Numer. Methods 11 (1995) 427–434.

[26] A.A. Yazdani, A. Gakwaya, G. Dhatt, An improved superconvergent patch recovery technique for the axisymmetrical problems, Comput. Struct. 66 (1998) 799–821.

[27] O.C. Zienkiewicz, B. Boroomand, J.Z. Zhu, Recovery procedures in error estimation and adaptivity, part I: adaptivity in linear problems, Comput. Methods Appl. Mech. Engrg. 176 (1999) 111–125.

[28] G. Bugeda, A new adaptive remeshing scheme based on the sensitivity analysis of the SPR pointwise error estimation, Comput. Methods Appl. Mech. Engrg. 195 (2006) 462–478.

[29] B. Boroomand, O.C. Zienkiewicz, Recovery procedures in error estimation and adaptivity, part II: adaptivity in nonlinear problems of elasto-plasticity behaviour, Comput. Methods Appl. Mech. Engrg. 176 (1999) 127–146.

[30] H. Gu, M. Kitamura, A modified recovery procedure to improve the accuracy of stress at central area of bilinear quadrilateral element, J. Soc. Naval Architects Jpn. 188 (2000) 486–496.

[31] H. Gu, Z. Zong, K.C. Hung, A modified superconvergent patch recovery method and its application to large deformation problems, Finite Elem. Anal. Des. 40 (2004) 665–687.

[32] Stampack©, A General Finite Element System for Sheet Stamping and Forming Problems, v7.0.0, Quantech ATZ, Barcelona, Spain, 2007. <www.quantech.es>.

[33] W.B. Castelló. Large Strain Analysis of Bidimensional Solids Using an Assumed Strain Triangle (in Spanish), MSc. Thesis, Nac. Univ. of Córdoba, Argentina, 2005.

[34] GiD©, The Personal Pre and Post Processor, version 8.1, CIMNE, Barcelona, Spain, 2007. <www.gid.cimne.upc.es>.

[36] J. Akin, Finite Element Analysis with Error Estimators, Butterworth-Heinemann, London, 2005.

[37] Abaqus©, Student Edn., version 6.6.2, Simulia, 2006. www.abaqus.com.

[38] F. Beltran, J.M. Goicolea, Large strain plastic collapse: a comparison of explicit and implicit solutions, in: D.R.J. Owen, E. Hinton, E. Oñate (Eds.), International Conference on Computational Plasticity (COMPLAS 2), vol. 2, Pineridge Press, Barcelona, Spain, 1989, pp. 1125–1136.

[39] P.A.R. Rosa, R.M.S.O. Baptista, J.M.C. Rodrigues, P.A.F. Martins, External inversion of thin-walled tubes using a die (in Portuguese), Revista Iberoamericana de Ingeniería Mecánica 8 (2004) 79–90.

[40] L.M. Taylor, E.B. Becker, Some computational aspects of large deformation rate dependent plasticity problems, Comput. Methods Appl. Mech. Engrg. 41 (1983) 251–278.